Single-Particle Hyperspectral Imaging Reveals Kinetics of Silver Ion Leaching from Alloy Nanoparticles

Alexander Al-Zubeidi‡,∇, Frederic Stein¶, Charlotte Flatebo‡,∇,||, Christoph Rehbock¶, Seyyed Ali Hosseini Jebeli,†,∇, Christy F. Landes‡,†,δ,∇,, Stephan Barcikowski¶,*, Stephan Link‡,†,∇,*

‡Department of Chemistry, Rice University, 6100 Main Street, Houston, Texas 77005, United States

∇Smalley-Curl Institute, Rice University, 6100 Main Street, Houston, Texas 77005, United States

¶Technical Chemistry I and Center for Nanointegration, Duisburg-Essen, University of Duisburg-Essen, Universitätsstraße 7, 45141 Essen, Germany

||Applied Physics Program, Rice University, 6100 Main Street, Houston, Texas 77005, United States

†Department of Electrical and Computer Engineering, Rice University, 6100 Main Street, Houston, Texas 77005, United States

δDepartment of Chemical and Biomolecular Engineering, Rice University, 6100 Main Street, Houston, Texas 77005, United States

ABSTRACT:

Gold-silver alloy nanoparticles are interesting for multiple applications, including heterogeneous catalysis, optical sensing, and antimicrobial properties. The inert element gold acts as a stabilizer for silver to prevent particle corrosion or conversely to control the release kinetics of antimicrobial silver ions for long term efficiency at minimum cytotoxicity. However, little is known about the kinetics of silver ion leaching from bimetallic nanoparticles and how it is correlated with silver content, especially not on a single-particle level. To characterize the kinetics of silver ion release from gold-silver alloy nanoparticles, we employed a combination of electron microscopy and single-particle hyperspectral imaging with an acquisition speed fast enough to capture the irreversible silver ion leaching. Single-particle leaching profiles revealed a reduction in silver ion leaching rate due to the alloying with gold as well as two leaching stages, with a large heterogeneity in rate constants. We modelled the initial leaching stage with a shrinking-particle model with a rate constant that exponentially depends on the silver content. The second, slower leaching stage is controlled by the electrochemical oxidation potential of the alloy being steadily increased by the change in relative gold content, and diffusion of silver atoms through the lattice. Interestingly, individual nanoparticles with similar sizes and compositions exhibited completely different silver ion leaching yields. Most nanoparticles released silver completely, but 25% of them appeared to arrest leaching. Additionally, nanoparticles became slightly porous. Alloy nanoparticles, produced by scalable laser ablation in liquid, together with kinetic studies of silver ion leaching, provide an approach to design the durability or bioactivity of alloy nanoparticles.

KEYWORDS: single-particle spectroscopy, plasmon resonance, nanosilver, laser-generated nanoparticles, corrosion

Understanding silver ion leaching from gold-silver alloy nanoparticles is a prerequisite to designing alloy nanoparticles with either unintended or intended silver ion release. On the one hand, slowing down silver ion leaching will increase the durability of a plasmonic alloy nanoparticle in sensing applications (*e.g.*, in bioassays) minimizing temporal shifts in plasmon intensity or wavelength.[1, 2] In heterogeneous catalysis, in particular under oxidic or acidic conditions, attenuated silver ion leaching will improve catalyst durability and recyclability.[2-5] On the other hand, silver ion release is intended to fight infections caused by bacteria, and the release kinetics will set the therapeutic window.[6, 7]

The anti-bacterial properties of silver have sparked interest in the use of silver-containing nanoparticles as anti-bacterial agents for *in vivo* applications.[8-11] Silver's anti-microbial action is generally attributed to silver ions, which cause damage to the cell membrane of bacteria, or are absorbed by the cell and damage the cell from the inside.[12-15] Silver ions are effective against most bacteria, including those resistant to anti-biotics, allowing silver to serve as a multipurpose anti-bacterial agent.[16, 17] Particular interest has been devoted to silver nanoparticles, or nanosilver, as a way to deliver silver ions to infected sites, or to prevent implant-associated infections. Nanoparticles embedded in infected tissue or dental fillings have been used to leach silver over time and continuously supply silver ions.[13, 14, 16, 18] Depending on factors like size and surface charge, nanoparticles can also interact directly with the bacteria to increase anti-bacterial properties of silver, either through contact killing or by delivering silver ions directly to the bacteria (*e.g.*, by adhering to the cell wall).[15, 19, 20]

Although promising results have been reported for the use of silver nanoparticles as anti-bacterial agents, silver nanoparticles are unstable and dissolve quickly, typically releasing their entire silver content in less than three days under physiological conditions

(burst release).[21-23] As a result, the anti-microbial properties of pure silver nanoparticles quickly wear out and the high overall silver ion concentrations are also toxic to mammalian cells, raising concerns for many *in vivo* applications.[24-26] The resulting therapeutic concentration window is rather narrow and even further reduced in the presence of serum proteins.[6, 7] Similar drawbacks may arise when silver nanoparticles are used in optical sensing purposes[1] or are utilized in catalysis[3-5] where corrosion due to silver ion release may critically impair their functional stability. Different methods have been explored to stabilize silver nanoparticles, such as alloying with another metal,[26, 27] surface functionalization with protecting ligands,[28] as well encapsulation in polyethylene glycol or polyvinylpyrrolidone.[13, 29] Alloying silver with gold allows precise control of corrosion as well as intended silver ion release and improves biocompatibility as well as significantly reduced toxicity in reproduction biology *in vitro* and *in vivo* experiments.[30, 31] Recent studies reported an improved biocompatibility and chemical stability by using gold-silver alloy nanoparticles instead of pure silver nanoparticles.[26, 27, 32-37] These studies also found that alloy nanoparticles remain effective against bacteria. However, little is known about the kinetics of silver ion release from individual alloy nanoparticles.[27, 33, 34] Ensemble studies directly comparing gold-silver alloy nanoparticles with pure silver nanoparticles produced conflicting results: Both slower and faster silver ion leaching was observed when gold or other transition metals were added to the composition of the nanoparticles.[33, 35] Interestingly, adding as little as 10-20 atom % of gold was reported to significantly decrease the silver dissolution rate.[38 39] To understand how composition affects silver ion leaching kinetics and to enable the design of nanoparticles that are capable of releasing silver ions in a controlled fashion, single-particle investigations are desperately needed to remove effects caused by nanoparticle heterogeneity and elucidate the release mechanism.

The properties of individual silver and gold-silver alloy nanoparticles can be monitored optically through their localized surface plasmon resonance, the collective oscillation of conduction band electrons in the metal nanoparticle. When plasmonic nanoparticles are illuminated, the plasmon leads to strong scattering and absorption of light.[40] The optical cross-sections of a plasmonic nanoparticle depend on its size, shape,[41, 42] and composition,[43-45] making it possible to monitor morphological changes optically. Wavelength and intensity changes in ensemble UV-vis spectra were used to monitor the dissolution of gold and silver nanoparticles,[15, 46, 47] as well as the silver ion leaching of gold-silver alloy nanoparticles.[48-50] However, the fact that leached silver ions cause nanoparticle aggregation in solution complicates optical ensemble methods.[23, 51, 52] Single-particle spectroscopy typically requires the immobilization of nanoparticles on a support substrate,[53, 54] thereby avoiding nanoparticle aggregation even under the harshest solution conditions. Dark-field spectroscopy is most commonly employed to study single plasmonic nanoparticles, but for monitoring time-dependent irreversible processes must be implemented in such a way that the acquisition of tens to hundreds of nanoparticles is fast enough to yield statistically relevant results.[55] Hyperspectral imaging can overcome this limitation and has been used as a non-invasive approach to track morphological changes, oxidation, and dissolution of individual nanoparticles with up to millisecond temporal resolution.[56-60]

In this work, we used hyperspectral dark-field imaging to monitor silver ion leaching from individual alloy nanoparticles synthesized by laser ablation in liquids. This synthesis route is well established for the generation of colloidal nanoparticles[61] and is scalable with productivities up to 4 g/h, equivalent to tens of liters colloid per hour.[62, 63] It has been frequently used for the generation of gold-silver alloy nanoparticles[64] with well-controlled composition and ultrastructure on a single-particle level.[65] Furthermore, these nanoparticles are completely free of organic additives and are electrostatically stabilized in solution by ion

adsorption.[66] Note that residual reactants of wet chemical synthesis such as citrate can influence the ion release.[67] Hence, laser-generated colloids constitute an ideally suited model system to formulate a two-stage leaching model. We monitored the plasmon resonance of individual silver and gold-silver alloy nanoparticles, immobilized on indium tin oxide (ITO) microscope slide, of different compositions in dilute nitric acid to promote silver ion leaching as a function of time. Spectral intensity changes were correlated with nanoparticle size and composition using scanning electron microscopy (SEM) and energy dispersive X-ray spectroscopy (EDX). By tracking the intensity changes over time, we created *in situ* single-particle leaching profiles that are well described when combining our kinetic rate model with Mie theory simulations.

RESULTS AND DISCUSSION

Particle Characterization Before Leaching

Spectra of individual gold-silver alloy nanoparticles were measured in deionized water and correlated to SEM and EDX measurements. A spectroscopic flow cell was assembled with alloy nanoparticles (20 mole% gold, 80 mole% silver) deposited on ITO and filled with deionized water (Figure 1a). An evanescent field created by total internal reflection (TIR) of white light from a halogen lamp was used to illuminate the nanoparticles. A color image of the field of view shows the individual nanoparticles as blue, red, and white scatterers (Figure 1b). Single-particle spectra were acquired for 46 nanoparticles by directing the scattered light to a spectrograph, which was scanned across the field of view (Figure 1c). Afterward, the cell was disassembled, and SEM and EDX measurements of the same nanoparticles revealed all particles were spherical, consistent with previous reports for nanoparticles created by laser ablation.[68, 69] The particles contained between 77% and 84% silver (Figures 1h and S1 in the supporting information (SI)), and did not form core-shell-

structures, in accordance with previous single-particle EDX analysis of laser-fabricated gold-silver nanoparticles,[65, 68] and further confirmed by our own STEM-EDX characterization that also revealed homogenous alloying of gold and silver (see below and SI for more details). Spectra, SEM images, and silver content of the representative nanoparticles highlighted in Figure 1b are shown in Figure 1 d-g. Smaller nanoparticles (Figure 1d, e) had narrower, blue-shifted spectra and appeared blue in the dark-field scattering image (Figure 1b). The spectra of larger nanoparticles were broader with red-shifted maxima (Figure 1f, g), appearing red and white in the color dark-field scattering image (Figure 1b). We measured the spectra of the same nanoparticles three times over a duration of 20 minutes and observed no spectral changes, confirming that the nanoparticles were stable under our conditions in water under light illumination (Figure S2).

Mie theory is well suitable to describe the spectra for nanoparticles with diameters smaller than 130 nm. Mie theory simulated spectra using the dimensions from SEM and dielectric functions for an alloy with 80% silver were calculated. Mie theory predictions gave a good match with experimental data for small nanoparticles, which only supported a dipolar plasmon mode (Figure 1d - f). In contrast, for larger nanoparticles, Mie theory predicted two overlapping plasmon modes, a lower energy dipolar mode at around 650 nm and a higher energy quadrupolar mode at 450 nm (Figure 1 g).[70] The experimental scattering spectrum of the larger nanoparticles in Figure 1g displayed these two modes, albeit less resolved in the simulations. Better agreement could potentially be achieved with more advanced simulation methods but at the expense of computational time and the need to fully characterize geometry and composition of all particles before, during, and after the experiments, a non-feasible task for our leaching studies.

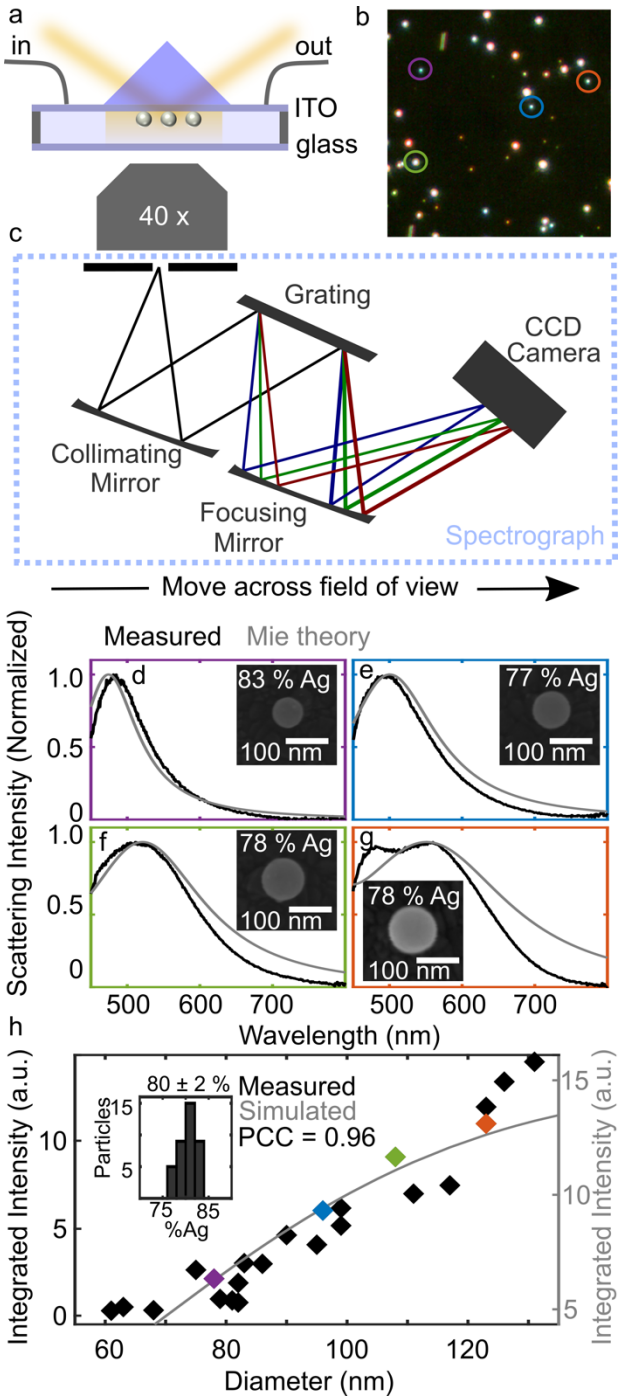

Figure 1. Hyperspectral imaging yields information about the size of gold-silver alloy nanoparticles, as illustrated here for the 80% silver alloy nanoparticles. (a) Illustration of a spectroscopic flow cell illuminated using prism TIR excitation. (b) Complementary metal–oxide–semiconductor camera color image of part of the investigated region. (c) Schematic representation of push-broom hyperspectral imaging. (d-g) Normalized scattering spectra of the nanoparticles highlighted in (b) overlaid with Mie theory simulations. Measured diameters were 78 nm, 96 nm, 108 nm, and 123 nm, respectively. The insets show the correlated SEM images and silver contents from EDX measurements. (h) Measured and simulated integrated spectral intensities as a function of nanoparticle diameter with the particles from (d-g) indicated by colored symbols. Only the 23 particles that were smaller than 130 nm are depicted because they had a well resolved dipolar plasmon resonance. The PCC between scattering intensity and

diameter is given by the legend. The y-axis of the simulated scattering intensities is adjusted to overlap with the experimental data according to a least-squares scaling approach. The distribution in silver content found by EDX is provided as an inset.

For *in situ* size analysis, we established first that integrated scattering intensities described particle size well, consistent with Mie theory simulations. The nanoparticles had a broad distribution in size with diameters ranging between 60 and 180 nm, while the silver content distribution was remarkably narrow, centered around 80% with a standard deviation of 2% (Figures 1h and S1). The scattering intensity integrated between 450 nm and 800 nm increased with nanoparticle size for particles smaller than 130 nm (Figure 1h), indicating that scattering intensity can be used as a measure of nanoparticle size. Mie theory predicted the same trend with a correlation of 0.96 between experimental and simulated scattering intensities (see SI section 3 for the calculation of the Pearson Correlation Coefficient (PCC)). For particles larger than 130 nm, Mie theory predicted no increase in scattering intensity as size increased, while our measured scattering spectra still showed intensity increases. These particles were excluded from the analysis, mainly because several plasmon modes start to overlap at this size range.

Detection of Silver Ion Leaching

Silver ion leaching from the same batch of 80% silver alloy nanoparticles was monitored optically and confirmed by correlated EDX. In another flow cell, spectra of 44 alloy nanoparticles (80% silver, 20% gold) were first measured in water. Three consecutive spectra were acquired, and then the water was replaced with 0.25 M aqueous nitric acid. As soon as the nitric acid was added, the scattering intensity of all spectra gradually decreased. By investigating nanoparticles immobilized on a substrate we were able to monitor the same nanoparticles over the entire duration of the leaching process without nanoparticle aggregation, which would have occurred in ensemble measurements under these acidic

conditions. To illustrate the decrease of the plasmon scattering intensity over a period of 4.5 hours, Figure 2 a-d provides four representative examples that are different from the particles studied in Figure 1. Correlated EDX of the same nanoparticles after dark-field spectroscopy revealed that the nanoparticles contained less silver than nanoparticles from the same sample batch not exposed to nitric acid (Figure 2 a-d insets), thereby confirming silver ion leaching by nitric acid. Final silver contents noticeably decreased from a starting value of 80 ± 2 % silver to a range between 53% and 78% silver, with a mean and standard deviation of 66 ± 6% silver (Figure 2e). These distributions differed with more than 99.99% confidence according to the Kolmogorov–Smirnov test (see SI section 4). The mean nanoparticle diameter also decreased slightly from 103 ± 28 nm to 96 ± 19 nm (Figure 2f), but these distributions were statistically similar ($p = 0.42$).

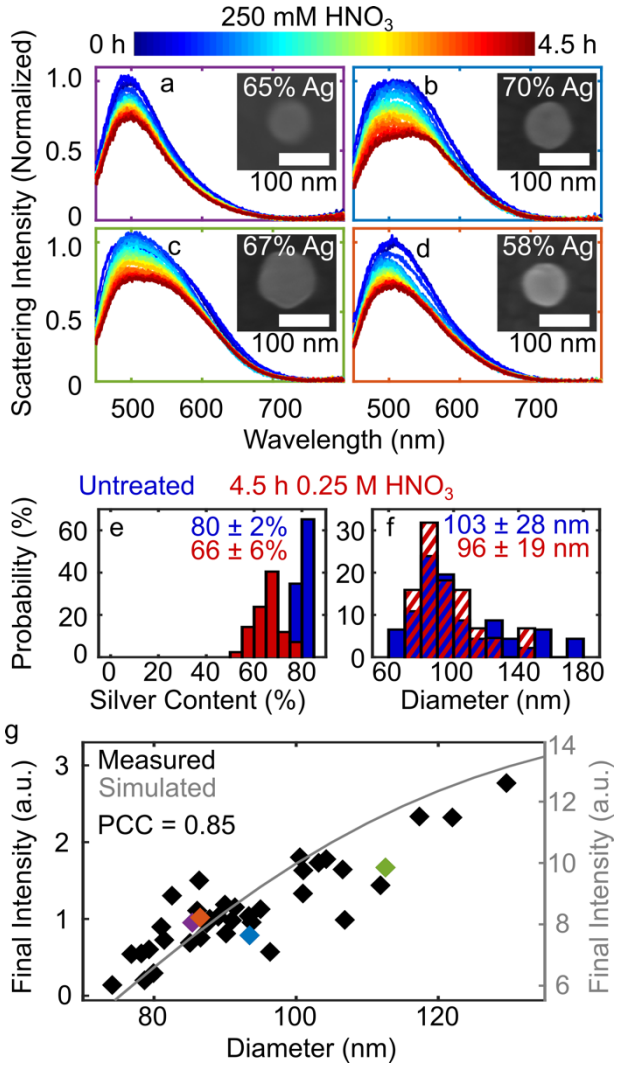

Figure 2. Nitric acid leaches silver ions from alloy nanoparticles. (a-d) Spectra of representative 80% silver alloy nanoparticles at different times after exposure to nitric acid. The insets show SEM images and silver content after the last spectrum was taken. The scale bars correspond to 100 nm. Measured diameters were 85 nm, 93 nm, 122 nm, and 86 nm, respectively. Intensities are normalized relative to the spectrum taken at 0 min. The differences in spectral width are likely due to slight variations in size, shape, and composition that are not captured in 2D SEM images. (e,f) Histograms of silver content and diameter, respectively, for particles that were leached and particles of another batch that was not leached, denoted as "no leaching" (same particles as in Figure 1). Note that because SEM has to be carried out after optical characterization it is not possible to study the same individual nanoparticles before and after leaching. (g) Measured and simulated integrated spectral intensities as a function of nanoparticle diameter after leaching, with the nanoparticles from (a-d) highlighted by colored symbols. The y-axis of the simulated scattering intensities is adjusted to overlap with the experimental data according to a least-squares scaling approach. 66% silver was assumed for the Mie theory simulations and the PCC is given in the legend. Absolute intensities cannot be compared between Figures 1h and 2g. Only relative intensity changes for the same sample cell can be compared.

Leached nanoparticles remained spherical but became slightly porous. Based on the average nanoparticle size and silver content before leaching and the average silver content

after leaching, the final particle size for a non-porous face-centered cubic sphere should be 85 ± 24 nm. However, the final measured size was 96 ± 19 nm, approximately 10% larger than expected, leading to the conclusion that nanoparticles became porous (see SI section 5). The SEM images in the insets of Figure 2a-d confirm that the nanoparticles were still spherical. No macroscopic porosity or pitting could be seen in SEM. However, atomic-scale porosity smaller than the resolution of our SEM cannot be excluded and is therefore likely. We expect that whether or not surface porosity can be observed depends mainly on the silver ion leaching rate. The rearrangement of atoms during leaching is a slow process that occurs over several hours.[71, 72] Under the mild leaching conditions presented in Figure 2, atoms were likely able to rearrange during the leaching process, filling most of the pores that would develop under accelerated kinetics, consistent with results shown below.

After silver ion leaching, the integrated scattering intensity still scaled with nanoparticle diameter and again agreed well with Mie theory calculations. Even though the nanoparticles became slightly porous based on the analysis above and had a wider distribution of silver content, the measured scattering intensity still increased with increasing nanoparticle size (Figure 2g). The final scattering intensity still showed good agreement with Mie theory (PCC = 0.85), indicating that we can still use Mie theory to approximate the scattering spectra for the low degree of porosity found here. To separately explore the effects of changing silver content and nanoparticle size, we simulated scattering spectra of 60 nm to 100 nm nanoparticles containing 80% silver and spectra of 100 nm particles containing 60% to 80% silver (Figure S3). As the diameter of the 80% silver particle was changed from 100 to 60 nm, the integrated scattering intensity decreased by approximately 80% of its initial value. Meanwhile, as the silver content of the 100 nm particle was changed from 80% to 60%, the integrated scattering intensity decreased by only 20%. Overall, decreasing nanoparticle size and silver content both lead to decreases in scattering intensity. However,

within the ranges considered here, the change in scattering intensity associated with the change in size dominated, explaining why the scattering intensity of leached nanoparticles still scaled well with the nanoparticle diameter, even though the final silver content varied. No statistically significant changes in peak resonance wavelength were observed in the measured spectra (Figures 2a-d, and S4). Mie theory simulations predict opposing trends: a smaller particle size results in a blue-shift (Figure S3);[73] a particle less rich in silver yields a red-shift.[43] While these factors work opposite to each other, it is important to stress that Mie theory does not fully capture the particle composition and structure, such as porosity and deviations from spherical shape.[74]

Effect of Silver Mole Fraction on Silver Ion Leaching

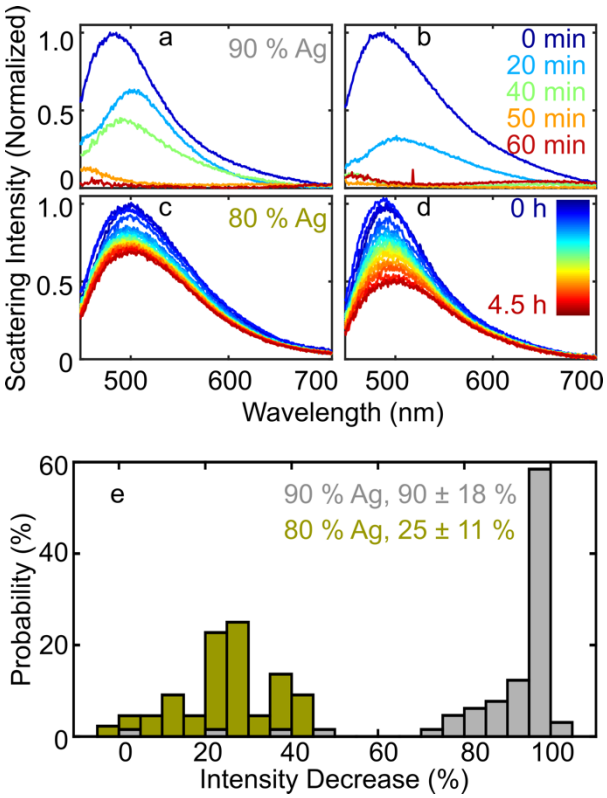

Figure 3. Silver content affects leaching. (a,b) Spectra of nanoparticles containing 90% silver before and at different times during leaching in 0.25 M HNO_3 (c,d) Spectra of nanoparticles from the same cell as shown in Figure 2, containing 80% silver before and at different times during leaching in 0.25 M HNO_3. Intensities are normalized to the spectrum taken at 0 min.

(e) Histogram of overall intensity change between the first and last spectra for both samples (65 particles for 90% silver alloy nanoparticles and 44 particles for 80% silver alloy nanoparticles were analyzed). Means and standard deviations of the intensity decrease are given in the legend. These distributions were statistically different ($p < 0.01$).

Increasing the initial silver content accelerated leaching. Another batch of alloy nanoparticles with approximately 90% silver was used to test the effect of silver content on leaching dynamics (see Figures S5 and S6 for characterization of this sample). Single-particle scattering spectra were tracked over a duration of 1 hour in 0.25 M nitric acid and revealed a more substantial decrease in scattering intensity, in some cases reaching the detection limit of our hyperspectral imaging system (Figure 3 a,b). By comparison, 80% silver alloy nanoparticles were still scattering strongly even after 4.5 hours of exposure to nitric acid (Figure 3c,d). As summarized in Figure 3e, the mean intensity decrease of the 90% silver alloy nanoparticles after one hour was 90 ± 18 % for 65 nanoparticles measured, with some nanoparticles completely invisible by dark-field spectroscopy. In contrast, the mean scattering intensity decrease of the 80% silver alloy nanoparticles was only 25 ± 11 % after 4.5 hours. Finally, chemically synthesized citrate capped silver nanoparticles (100 ± 7 nm, see Figure S7 for size characterization) dissolved beyond the detection limit after only 10 minutes in 0.25 M nitric acid, as shown in Figure S8. The strong dependence of leaching rate on silver content can be understood in terms of the activation energy for a silver ion leaving the alloy lattice.[38] If all bonds are silver-silver bonds, dissolution is rapid. However, as more gold-silver bonds are present, dissolution becomes increasingly challenging. The addition of gold thus decreases the rate of silver dissolution.[75]

Kinetics of Silver Ion Leaching

Integrated scattering intensities were used to create single-particle leaching profiles. Having established that integrated scattering intensity scales with nanoparticle diameter and

extent of leaching, we created time-resolved single-particle leaching profiles by plotting the integrated scattering intensity against time for the 80% silver alloy nanoparticles. Figure 4a-d displays the integrated scattering intensity as a function of acid exposure time for the same nanoparticles as given in Figure 2a-d. The first data point at time zero corresponds to the mean of the three spectra measured in water, with the standard deviation given as an error bar. After 0.25 M nitric acid was added, an initial rapid decrease in scattering intensity was seen. At later times, leaching slowed down based on the smaller changes in scattering intensity. The integrated scattering intensity never reached a plateau, indicating that leaching was still occurring at the end of the measurement, albeit slowly. Time-resolved leaching profiles for all nanoparticles had similar shapes and can be found in the SI (Figure S9).

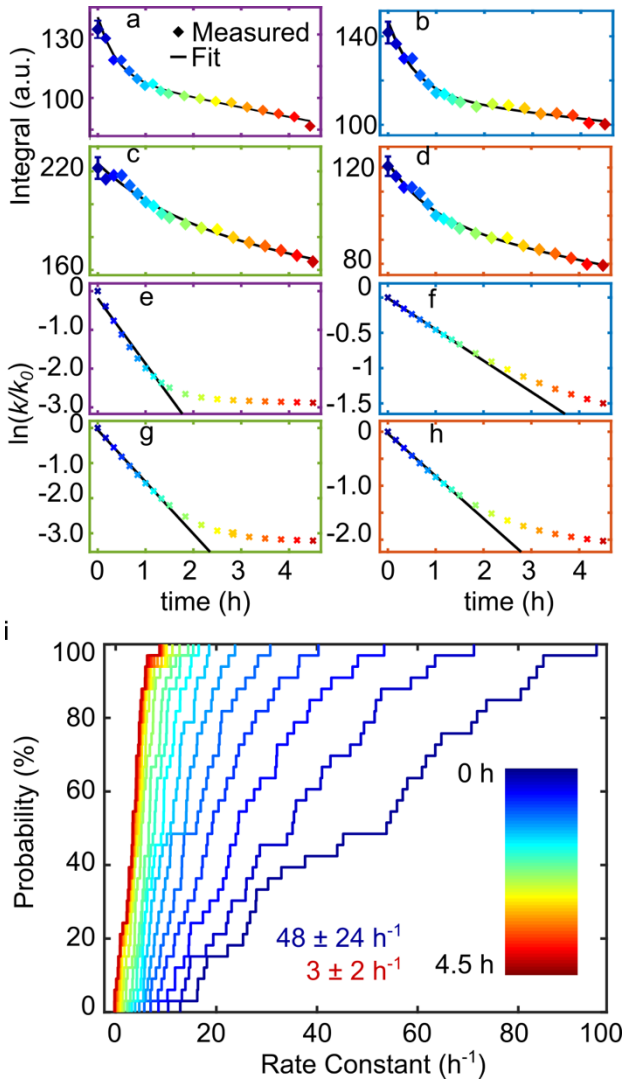

Figure 4. Silver ion leaching rate decreases over time. (a-d) Leaching profiles created by plotting the integrated scattering intensity against exposure time to nitric acid together with biexponential fits for representative 80% silver alloy nanoparticles. The frames are color-coded to Figure 2 (a-d) to indicate that the same nanoparticles are again highlighted here. The first data point is the mean of three spectra collected in water before acid was added, and the error bar is the corresponding standard deviation. (e-h) Natural logarithm of rate constant, obtained by taking the derivative of the fit at each time point for the nanoparticles shown in (a-d) and normalized by the rate constant at time zero, k_0. Note the initial linear regime, followed by the deviation from linearity at later times when the silver mole fraction is lower. The black lines are linear fits to the initial leaching stage. (i) Cumulative distribution functions of the leaching rate constant evaluated at different times, as indicated by the color scale bar. The means and standard deviations of the initial and final rate constants are displayed as insets.

Leaching rate constants extracted from the leaching profiles decreased over time, a behavior that cannot be explained by first order leaching kinetics. A single exponential fit cannot describe the experimental leaching profiles, indicating a more complex mechanism.

Under less harsh conditions, Hahn *et al.* also experimentally observed a slow-down of silver ion release from laser-generated silver nanoparticle polymer composites immersed in distilled water for 1-42 days at 37°C. This long-term metal ion release was best described by pseudo-first-order kinetics to which first order and second order fits gave similar residuals.[76, 77] Here, a biexponential fit was applied to label the shape of the leaching profiles phenomenologically. This fit gave excellent agreement with the experiment for the leaching profiles of almost all nanoparticles. (Figures 4a-d and S9). The derivative of the biexponential fit at each time point, instead of the noisier experimental data, was taken to extract the slope and thus an effective leaching rate constant, k (Figure 4e-h). This effective rate constant normalized by the rate at time zero, k_0, decreased with time initially exponentially as demonstrated by the good agreement with the fits given by the black lines in Figure 4e-h. After about two hours, the leaching rate constant decreased more slowly. The cumulative distribution functions of the rate constants for all nanoparticles investigated at different experimental time point in Figure 4i demonstrate a more than ten-fold decrease in the rate constant over 4.5 hours from 48 ± 24 h^{-1} to 3 ± 2 h^{-1}. Notably, the cumulative distribution functions illustrate the large standard deviation for the measured rate constant, especially at early times, partially caused by a combination of differences in initial particle composition and nanoparticle size. Despite a relatively narrow distribution in initial silver composition ranging from 77% to 84% (see Figure S1), such small changes likely had a large effect when considering the significant differences seen in Figure 3 for 80% *vs.* 90% silver alloy nanoparticles. In previous work, some authors found that small particles leached faster.[22, 23, 78] However, we observed only a weak correlation between particle size and leaching rate (Figure S10). Other factors such as slight differences in crystallinity might have also contributed to the differences in reactivity,[58, 79, 80] and further studies are needed to fully

understand the observed heterogeneity in silver ion leaching kinetics. This result clearly demonstrates the need for a single-particle spectroscopy approach as undertaken here.

Reductions in leaching rates were described in the literature before for elemental silver nanoparticles and were typically attributed to nanoparticle aggregation or solubility issues when the solution reached the solubility limit for silver ions.[23, 81, 82] Nanoparticle aggregation was not an issue here because the particles were immobilized on a substrate. We also used a relatively low nanoparticle density (~10^6 particles per cm^2), resulting in a maximum silver concentration of about 1 μM, which is orders of magnitude below the solubility limit of silver nitrate (see SI section 13 for further details).[83] Additionally, if leaching was limited by the solubility of silver ions, the pure silver nanoparticles should not have leached completely either. Decreases in rates over time were also reported for mass transport limited leaching because a growing diffusion layer around the nanoparticle slows down leaching by reducing the supply of oxidants.[84] However, if the reaction here was mass transport limited with respect to the oxidant, all three samples should have leached at the same rate independent of silver content. Instead, we observed increased leaching rate constants with increasing silver content in the gold-silver alloy nanoparticles. Note that the 90% silver alloy and pure silver nanoparticles leached so quickly after exposure to nitric acid that we were not even able to accurately quantify the corresponding rate constants.

We, therefore, propose a two-stage model to describe silver ion leaching from alloy nanoparticles. It is known that leaching of silver ions from homogenous gold-silver alloys can occur *via* two distinct mechanisms depending on the initial composition.[38] In the case of an alloy containing more than 65% silver, the material contains no continuous lattice of gold atoms, and dissolution of silver atoms is determined by the activation energy of silver atoms leaving the lattice.[38, 75, 85] The reaction is then dominated by the dissolution of silver on the nanoparticle surface. By measuring silver ion leaching from alloy films of different

compositions, Espiell and coworkers found that for an alloy containing more than 65% silver the leaching rate depends exponentially on the silver mole fraction of the alloy.[38] For an alloy containing less than 65% silver, gold atoms start to dominate the lattice.[38, 75, 85] After the first few silver atoms that are on the surface leave the lattice, additional leaching requires the diffusion of silver atoms through a gold-rich lattice to reach the surface.[72, 75, 86] On the other hand, when a gold-silver alloy contains 90% silver,[38] isolated atoms or pairs but no continuous structures of gold are found, explaining the absence of the second leaching stage for such particles. Note that most literature on the crystal structure is based on thin films or wet chemically-prepared gold-silver alloy nanoparticles. Co-precipitation synthesis in thermodynamic equilibrium has been reported to cause significant enrichment of gold in the core of the gold-silver alloy nanoparticles.[87] In contrary, laser synthesis is a non-equilibrium, kinetically controlled method that results in monophasic gold-silver alloy nanoparticles with crystal lattice constants that strictly follow Vergard´s law along the whole mole fraction range.[68] But recent synchrotron X-ray absorption spectroscopy indicates that there is a slight enrichment of the respective less abundant element in the surface region of the nanoparticle (silver-rich gold-silver alloy nanoparticles show enrichment of gold near the surface and *vice versa*).[88] In contrary, in-depth investigation of chemically prepared gold-silver alloy nanoparticles with varying mole fractions clearly revealed that the particles form a solid solution alloy with enrichment of silver on the nanoparticle surface, independent of the alloy composition.[89]

We thus propose a two-stage leaching model for gold-silver alloy nanoparticles. Initially, the leaching rate is controlled by the oxidation and dissolution of silver on the surface, characterized by a rate constant that depends exponentially on the silver mole fraction. As more silver dissolves, the nanoparticle becomes richer in gold, and the rate constant decreases exponentially with silver content. Eventually, the lattice is rich enough in

gold that a second leaching stage sets in. In this second leaching stage, the effective leaching rate constant is controlled by the diffusion of silver atoms through the lattice. In addition, the electrochemical potential of the nanoparticle will change along with the change in silver mole fraction in the particle during silver ion release, making further oxidation of the gold-enriched particle more difficult.[75, 90] The equilibrium potential, E_{equil}, for leaching a silver atom from the surface of an alloy is described by:[72]

$$E_{equil}(x_{Ag}) = E_{Ag^+/Ag} - \frac{\mathrm{R}T}{\mathrm{F}} \ln(a_{Ag}) \quad (1)$$

Here $E_{Ag^+/Ag}$ is the equilibrium potential of elemental silver, R is the ideal gas constant, T is the temperature, F is Faraday's constant, and a_{Ag} is the activity of the silver atoms in the alloy.[72] The oxidation potential of a gold-silver alloy therefore increases to more anodic potentials as the silver content decreases. Accordingly, cyclic voltammetry showed silver oxidation peak shift to higher potentials along with oxidation peak shift broadening with decreasing silver molar fraction in the gold-silver alloy nanoparticles.[89] This transition between leaching stages agrees reasonably well with our EDX measurements, which indicated that after 4.5 hours the alloy nanoparticles contained significantly less (66 ± 6 %) silver, close to the reported 65% threshold below which lattice diffusion begins to dominate.[38, 75, 85] There is heterogeneity in the onset of the second leaching stage with respect to the time and silver percentage, with some particles exhibiting deviations from linearity in $\ln(k/k_0)$ as early as 1.5 hours (Figure 4e) and others as late as 2.5 hours (Figure 4f). Also, some particles entered the second stage but still contained more than 70% silver after disassembling the cell, while others contained as little as 53%.

Theoretical Modelling of Leaching Kinetics

To quantitatively describe the first leaching stage, we propose a shrinking-particle model with a rate constant that exponentially depends on the silver mole fraction,

schematically illustrated in Figure 5a. Assuming the reaction rate is first order with respect to proton concentration and surface area,[38] the change in nanoparticle volume is given by:

$$\frac{dV}{dt} = -\, k_1\, SA\, [H^+] \tag{2}$$

Here, $V =$ volume of sphere, $t =$ time, $SA =$ surface area of sphere, $k_1 =$ rate constant, and $[H^+] =$ proton concentration. From equation (2), the following rate law can be derived for a bimetallic nanoparticle with only one component dissolving (see SI section 14 for derivation of equation (3) from equation (2)):

$$d(t) = d_0\ - k\, t\, [H^+] \tag{3}$$

Here, $d =$ diameter of particle, $d_0 =$ initial diameter of particle, and $k =$ rate constant. k_1 and k are related to each other through a constant of proportionality (see SI). We next assume that k depends exponentially on the silver mole fraction, x_{Ag}, according to:

$$k = k_0 \exp\left(x_{Ag}\right) \tag{4}$$

With an initial rate constant k_0 and a time-dependent silver mole fraction $x_{Ag}(t)$, Equations (3) and (4) then yield:

$$d(t) = d_0\ - k_0 \exp\left(x_{Ag}(t)\right) t\, [H^+] \tag{5}$$

Simulated kinetics using the proposed rate model reproduced the initial leaching stage. A 100 nm nanoparticle with a silver mole fraction of 0.8 was taken as the starting point. The diameter and silver mole fraction after a timestep of three minutes (hyperspectral image acquisition time) was simulated using equation (5) and the mean initial rate constant from experiments (48 h^{-1}). The effective rate constant was updated using equation (4), and the diameter and silver mole fraction were calculated for the next timestep. This process was continued until the nanoparticle contained no more silver (see SI section 15 for more details). Figure 5b illustrates the change in nanoparticle diameter over time, with the changing silver mole fraction displayed in the inset. These nanoparticle diameters and silver mole fractions at

each time point were used to simulate Mie theory scattering spectra (Figure 5c). The integrated spectral intensity reproduced the shape of the initial leaching stage well (Figure 5d), despite ignoring small degrees of particle porosity in these simulations. In particular, the logarithm of the normalized simulated rate constant as a function of time (Figure 5d inset) revealed the same exponential trend as the normalized experimental rate constant for the initial leaching stage (Figure 4 e-h). The exponential change in rate can be understood through the silver mole fraction, which changes linearly over time. Equation (4) hence predicts an exponential decrease in reaction rate. Complete leaching was predicted over a duration of five hours. In the experimental case, complete leaching was not seen after a similar time since the second, slower, leaching stage started to dominate after about 2.5 hours. The second leaching stage is not captured by the rate model as the rate model only treats the case of a surface reaction limited rate.

The more commonly used shrinking-particle model does not describe silver ion leaching from our alloy nanoparticles. Leaching kinetics for a shrinking-particle model were simulated again by applying the initial rate from experiments to a 100 nm nanosphere. However, the rate constant was not updated after each timestep and the dissolution was hence modelled with a constant rate constant. As illustrated in Figure 5e, the nanoparticle diameter changes linearly with time, as expected for a shrinking-particle model,[91] while the silver mole fraction changes logarithmically (Figure 5e inset). The integrated scattering intensity obtained from the simulated spectra (Figure 5f) decreases mostly in a linear trend, not describing the experimentally observed behavior. The shrinking-particle model furthermore predicts faster dissolution, with complete dissolution occurring after only 2.5 hours. Furthermore, considering that our experimental results suggest minor changes in particle size, we also explored an alternative rate model in which the particle size remained constant (see SI section 16). That approach yielded worse agreement (Figure S11), suggesting that changes

in size together with a decreasing silver mole fraction must be considered. We acknowledge that our model based on Mie theory simulations presents a simplified idealization, which adequately captures the initial leaching kinetics though.

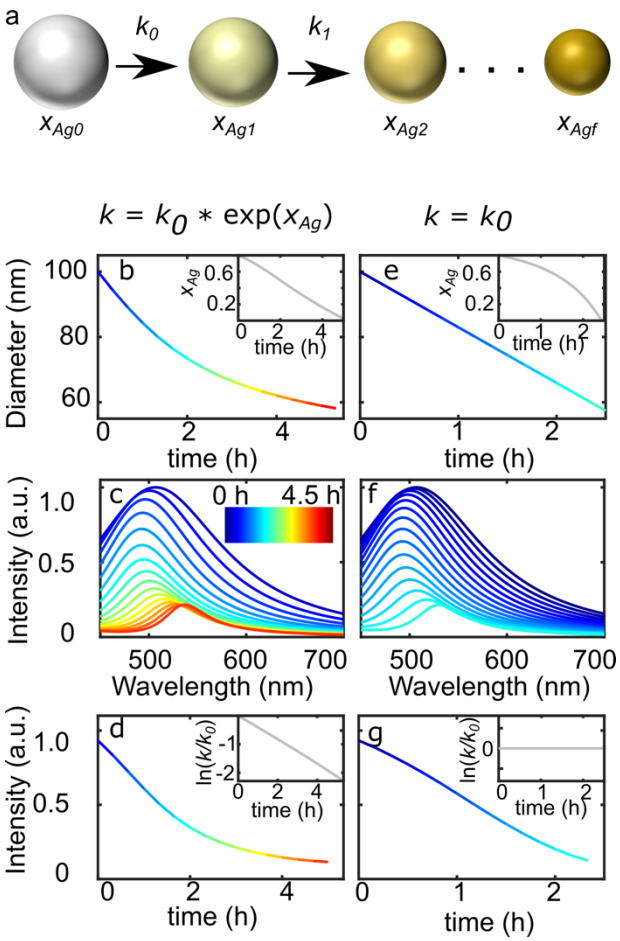

Figure 5. Proposed leaching mechanism with changing rate constant. (a) Schematic illustration of the shrinking-particle model with changing mole fraction and rate constant. (b) Simulated diameter over time for a sphere with an initial diameter of 100 nm and 80% silver content using the mean of the experimentally found initial rates with the proposed mole fraction dependent rate constant. The inset shows the silver mole fraction over time. (c) Mie theory spectra as a function of time for the nanoparticles in (b). The high gold content towards the end of leaching causes a red-shift of the plasmon resonance.[43] (d) Simulated leaching profiles using the spectra in (c). The inset shows the natural logarithm of the rate constant over time. (e) Simulated diameter and silver mole fraction (inset) using the mean of the experimentally found initial rates without the proposed mole fraction dependence. (f) Simulated spectra from the particle sizes and mole fraction in (e). (g) Simulated leaching profiles and the natural logarithm of the normalized rate constant using the spectra in (f). Additional details regarding the simulations are given in section 13 of the SI.

Porosity and Surface Passivation

Complete leaching was possible for some nanoparticles, while others barely lost any silver, an important property that was only resolved by our single-particle approach used here. In the previous experiments, we stopped silver ion leaching while the nanoparticles still had more than 50% silver. Prior studies found contradicting results for complete silver ion leaching, with some studies observing that alloys can leach completely, while others found that it was impossible to leach alloys that were more than 55% gold.[38, 49, 72] To test whether or not 80% silver nanoparticles are able to completely release their silver content, we repeated our experiments using 1.7 M nitric acid. We monitored the nanoparticle scattering spectra for three hours (Figures 6a-d and S12), followed by correlated SEM and EDX measurements. The average scattering intensity decreased by 68% and the average silver content dropped from 80% silver to 18% silver, with 60% of nanoparticles no longer containing any detectable levels of silver (Figure 6e, f). The higher acid concentration explains the faster leaching kinetics.[38] The distributions of scattering intensity decrease and final silver content were broad, spanning the entire range, hence illustrating the heterogeneity in silver ion leaching from alloy nanoparticles (Figure 6). Specifically, three main cases can be seen from the distributions: Ten nanoparticles exhibited little to no change in scattering intensity and contained more than 50% silver (Figure 6a). Seven nanoparticles showed strong changes in scattering intensity and still contained between 7% and 20% silver (Figure 6b). The remaining 26 nanoparticles contained no detectible traces of silver (Figure 6c, d), and many of them no longer had detectible scattering spectra.

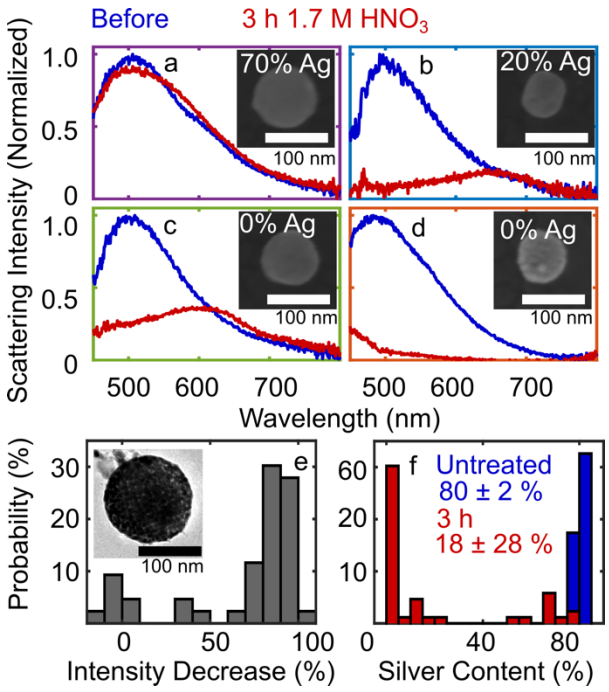

Figure 6. Complete silver ion leaching is possible for most nanoparticles in 1.7 M nitric acid. (a-d) Representative spectra before and after exposure of 80% silver alloy nanoparticles to 1.7 M nitric acid for three hours. The insets show SEM and EDX analyses after leaching. (e) Histogram of intensity change after three hours of silver ion leaching (68 ± 39%). The inset shows a brightfield TEM image of a particle leached for 45 minutes in 1.7 M nitric acid. (f) Histogram of silver content obtained from EDX for all 43 nanoparticles after leaching. EDX data for 46 different nanoparticles from the same sample that were not exposed to nitric acid is shown for comparison. Only 30% of particles still had well defined spectra after leaching, while the rest did not contain enough metal to be optically detected.

The particles that leached completely or nearly completely showed evidence for porosity, in agreement with our analysis above under milder leaching conditions as well as previous reports.[49, 50, 72] The expected final diameter of the nanoparticles was 64 ± 19 nm (SI section 5), yet the measured size was 93 ± 19 nm, again indicating porosity (Figure S13). While we were unable to detect direct evidence for porosity in the SEM images for the 80% silver alloy nanoparticles leached in 0.25 M nitric acid, the greater extent of leaching and higher leaching rate in this experiment allowed us to do so. 25 of the 33 nanoparticles that contained less than 50% silver had rough surfaces as evidenced by the SEM images shown in Figures 6d and S14. Furthermore, those nanoparticles that were still detectible optically had final peak resonance wavelengths between 650 and 750 nm. Although a small red-shift is expected due to loss of silver,[49, 50, 92] the red-shifts observed here cannot be explained entirely

by a change in composition as Mie theory predicts a peak resonance wavelength of 570 nm for a 100 nm pure gold nanoparticle. These greater red-shifts are therefore further evidence for surface roughness and porosity.[50] Visible surface roughness and spectral red-shifts only occurred in particles that contained less than 50% silver. The ten nanoparticles that contained more than 50% silver remained smooth spheres and appeared similar to what was observed under the milder leaching conditions presented in Figure 2. The TEM image in Figure 6e for a representative particle leached under similar conditions revealed more evidence for porosity, and high-resolution STEM-EDX mapping confirmed that particles became porous (Figures 7 and S15). Lattice rearrangement as a result of surface diffusion reduces the extent of porosity for a slow leaching process. However, as lattice rearrangement takes hours,[71] the fast silver ion leaching in 1.7 M nitric acid led to more porosity, consistent with previous reports on electrochemical dealloying.[72]

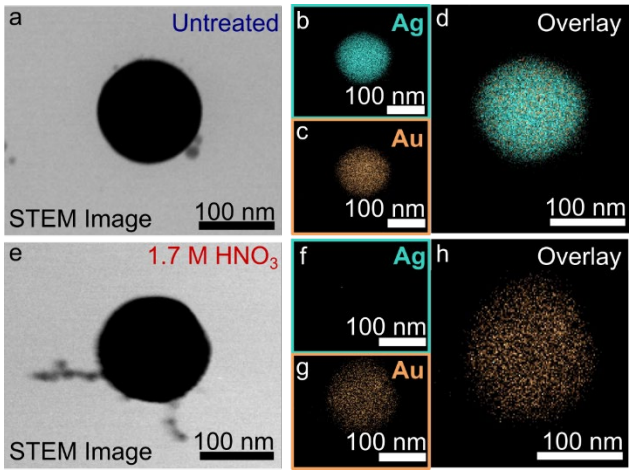

Figure 7: STEM-EDX characterization of alloy nanoparticles. (a-d) STEM-EDX maps of a representative untreated alloy nanoparticle (80% silver). (e-h) STEM-EDX maps of a different representative nanoparticle after leaching in 1.7 M nitric acid for 45 minutes revealing complete loss of silver and atomic level porosity. Note that these measurements, unlike correlated SEM imaging, were not correlated with optical spectroscopy, as such experiments would require a new sample cell design first.

The spectra of ten particles that contained more than 50% of silver no longer changed after the first ten minutes (Figure S12). We conclude that leaching had reached its final stage in 1.7 M nitric acid because this subset of nanoparticles became hindered in dissolution. We

did not observe the formation of a distinct passivation layer (such as a shell built-up or shell segregation) or significant gold enrichment on the surface though. In the literature, passivation has been explained either by layer or pore formation, and also electrochemical effects have to be taken into account.[72] Specifically, passivation to leaching has previously been attributed to gold rich layers on the surface, which form as the lattice rearranges.[71, 93] In the case of gold-silver alloy films, whether or not a passivation layer is formed depends on the leaching rate: when the silver is leached out of the alloy quickly enough that emerging pores are not filled by surface lattice diffusion, the pores allow percolation of lixiviant into the alloy and complete leaching is possible.[72, 86] However, when silver is leached more slowly pores are filled and no percolation is possible.[72, 86] This mechanism is consistent with our observation that particles that became porous lost their silver content, while particles that appeared passivated were less porous. In electrochemical studies this passivation threshold is characterized by a critical potential.[72, 86] In our case, there is no clear threshold similar to the critical potential, indicating that the occurrence of passivation is heterogeneous in nanoparticles. This heterogeneity was also observed in a recent study by Tschulik and co-workers, where the electrochemical leaching of silver ions from gold-silver alloy nanoparticles (80% silver) was investigated.[93] The authors found that 10% of particles remained rich in silver after leaching.[93]. In addition, the electrochemical potential of a particle that undergoes leaching is expected to increase, as it is enriched in gold molar fraction during silver release.

Outlook on Biological Applications

Silver ion leaching in biological *in vitro* applications typically is studied in less acidic bacterial growth media or buffer solutions with pH between 5.6 and 7.9.[8, 13] But acidic pH is known to be caused by infections,[94, 95] such as implant-associated infections. Furthermore,

lysozymes, known to trap nanoparticles in eukaryotic cells by curvature effects,[96, 97]naturally have low pH.[98, 99] Hence, the more acidic conditions mimic the lower pH milieu in the situations relevant to antibacterial implant coatings or cytotoxicity after endosomal uptake. We chose nitric acid to promote silver ion leaching in order to monitor kinetics of silver ion release on experimentally accessible time scales. Our findings are in good accordance with previous toxicological examinations of laser-fabricated gold-silver alloy nanoparticles.[30, 37] While silver ion leaching is likely slower under less harsh physiological conditions, the mechanistic insight from the current studies is important for several reasons. First, there is a need to consider heterogeneity in silver ion release rates because effects on bacteria and fibroblast growth as well as oocyte maturation have been reported to be non-linearly correlated with the gold molar fraction.[30, 37] Next, passivation effects by alloying of silver with gold, as we conclude here, are also important for biological outcomes.[30, 37] In bioassays with laser-generated gold-silver colloids, particles that contained 50% silver and 50% gold displayed similar bioactivity as pure gold, no matter if tested in microbiology, or even in reproduction biology.[31, 37] Overall, bioactivity of silver nanoparticles is known to be significantly decreased by alloying with gold. [30, 31, 37] In other words, a given mass dose of silver is more toxic if presented as elemental silver compared to a silver equivalent higher mass dose of gold-silver alloy nanoparticles. However, particle specific effects, such as adhesion to the cell wall, remain for alloy nanoparticles.[27]

CONCLUSIONS

In summary, we demonstrated the use of single-particle hyperspectral imaging combined with SEM and EDX to quantitatively characterize the time-resolved leaching of silver ions from gold-silver alloy nanoparticles created by laser ablation in liquid. By tracking changes in scattering intensity, we found that alloying silver particles with gold strongly

affects leaching rates. Initial leaching rates were heterogeneous, likely due to differences in particle ultrastructure or silver content, with a small contribution from differences in nanoparticle size, highlighting the importance of a single-particle approach. Leaching rates decreased over time for alloy nanoparticles as the particles became less rich in silver. Two leaching stages were found, an initial fast stage when the gold-silver alloy nanoparticles bear high silver content, followed by a slower stage when the lattice of the nanoparticles contained similar amounts of gold and silver. We described the initial stage with a kinetic model, in which the rate constant exponentially decreased with the silver mole fraction of the nanoparticle. With this approach as input for Mie theory simulations of scattering spectra, we successfully reproduced the shape of the experimental leaching profiles. We attribute the second, slower leaching kinetic stage where the alloy nanoparticles are enriched with gold to the slower diffusion of silver ions through the lattice of gold atoms and the shift in the particles' electrochemical potential to higher values. We found that mainly nanoparticle composition and proton concentration affected the leaching rate. Under more acidic conditions in 1.7 M nitric acid the entire silver content leached almost completely for most nanoparticles within ten minutes, creating rough and porous gold spheres with red-shifted plasmon resonances. However, almost 25% of the nanoparticles still contained more than 50% silver and were stable for at least three hours, likely due to the formation of passivating diffusion barriers made of gold additionally increasing the electrochemical potential for silver oxidation. These findings will help to elucidate the dissolution mechanisms of gold-silver alloy nanoparticles relevant not only for antimicrobial studies but also for corrosion stability of silver-based nanoparticles in heterogeneous catalysis and for plasmonic sensing in an aqueous environment. Interestingly, even under harsh acidic conditions, the silver dissolution strongly slowed down, if there was enough gold in the starting alloy. This 50:50 gold-silver alloy seems to be quite stable against further change in composition for a subset of particles,

a prerequisite for high durability in catalysis or long-term use in plasmonics. Even though we used acidic environments to promote the dissolution behavior it is conceivable that similar effects may occur in biological media and their time constants may also be detectable by hyperspectral single-particle spectroscopy, though much slower kinetics and much longer measurement times would be expected.

METHODS

Alloy nanoparticle preparation: Alloy nanoparticles were produced by laser ablation using a previously reported technique.[68] Briefly, laser induced spherical nanoparticle ablation was carried out with a picosecond laser (Atlantic 532, Ekspla) at a wavelength of 1064 nm, a pulse duration of 10 ps, a pulse energy of 160 mJ, and a repetition rate of 100 kHz. Laser light was directed to gold-silver alloy films (Research Institute for Precious Metals and Metal Chemistry, Schwäbisch Gmünd) with a 100 mm focal distance lens. The composition of the alloy films determined the silver mole fraction of the resulting alloy nanoparticles. Centrifugation was used to separate out smaller particles that could not be detected by dark-field spectroscopy. The nanoparticles were synthesized, dispersed, and stored in 100 μM aqueous NaCl solution.

Spectroscopic flow cell preparation: Two holes were laser cut diagonally across an ITO coated coverslip (50mm x 75mm x 0.9-0.1mm, ECI#949, Evaporated Coatings Inc.). The coverslip was cleaned by sonicating in soapy water for 10 minutes, followed by plasma cleaning for two minutes. Alloy nanoparticles were then spin-coated onto the ITO coated side of the cleaned coverslip. A double-sided adhesive spacer (0.12 mm thick, SA-S-1L, Grace Bio Labs) with a laser cut flow channel was placed on the coverslip and aligned with the laser cut holes. A second spacer with a laser cut flow channel was placed on top, keeping the thin protective plastic film on the side facing the other adhesive spacer. This approach allowed us

to pull the cell apart after spectroscopic experiments for further analysis by SEM. A second coverslip (50mm x 75mm x 0.9-0.1 mm, Brain Research Laboratories) was placed on top, and the assembled cell was secured using an aluminum frame. Tubing was attached to the holes, creating a flow cell. The flow cell was filled with Milli-Q water and placed on the microscope. Spectra were taken in water, then the water was replaced with aqueous nitric acid (99.9% pure, Alfa Aesar). For correlated spectroscopy, a pattern was cut into the ITO using a focused ion beam (30 kV, 0.23 nA, dwell time 1 µs, Helios NanoLab 660, FEI) before depositing nanoparticles. After dark-field spectroscopy, the cell was rinsed with Milli-Q water and emptied. The ITO coverslip was then first reinforced by sticking it to a thick microscope slide using double-sided tape. Duct tape was attached to the other coverslip without nanoparticles, making it possible to carefully peel it off from the cell. The nanoparticles on the remaining ITO coverslip were rinsed again with Milli-Q water, dried under nitrogen, and immediately investigated by SEM.

Single-particle spectroscopy: The flow cell was placed on an inverted microscope (Axio Observer, Zeiss) with the ITO coverslip facing up. Light from a quartz tungsten halogen lamp (66884, Newport) was sent through a 304−785 nm bandpass filter to remove infra-red light (FGS550, Thorlabs), collimated and focused by two identical planar convex lenses (AC254-030-A, Thorlabs), and directed through a prism at approximately 55º to create TIR (Figure 1a). The resulting evanescent wave excited the nanoparticles, and the scattered light was collected using a 40x air spaced objective with a numerical aperture of 0.6 (LD Plan-Neofluar 40x/0.6 Corr, Zeiss). The light from the objective was either directed to a camera (MU300, Amscope) to collect a color image of the particle positions (Figure 1b) or to a spectrograph (Acton SpectraPro 2150i, Princeton Instruments) mounted on a scanning stage driven by a linear actuator (LTA-HL, Newport; Figure 1c). A slit at the image plane allowed only a vertical slice of light to reach the spectrograph. That image slice was collimated, directed to a

diffraction grating (300 grooves per millimeter), and focused onto a charge-coupled device detector (PIXIS BR 400, Princeton Instruments), yielding spectra for each vertical position in the image slice. Spectra for the entire region of interest were collected by moving the spectrograph across the entire field of view. An exposure of two seconds was used for each step and scanning the field of view took about seven minutes. The next image was started in 10 minute intervals following a manual focus adjustment to correct for sample drift. This procedure was needed especially for measurements taking several hours, but introduced an error much smaller than the changes observed due to silver ion leaching (see Figure S2 for further discussion). None of the spectra were averaged. A typical hyperspectral data cube was 300 x 100 pixel with a 0.8 nm spectral resolution, covering an area of approximately 150 x 50 µm. Spectral information was extracted by summing across a 5x5 pixel area, subtracting background intensity using a nearby area with the same number of pixels but containing no nanoparticle, and dividing by the spectrum of the halogen lamp, from which the dark counts of the detector were subtracted.

SEM: SEM imaging (Helios NanoLab 660, FEI) was carried out at 10 kV and 0.4 nA with a dwell time of 1 µs. EDX measurements (X-mMax^N 80, Oxford Instruments) were taken over an area completely containing an individual nanoparticle with the same instrument and beam settings using a two minute acquisition time.

TEM: Citrate stabilized silver nanospheres (BioPure Silver Nanospheres – Bare, nanoComposix) were drop cast on a copper grid (EMS300-Cu, Electron Microscopy Sciences) and dried under ultrapure nitrogen in a desiccator. Brightfield TEM micrographs were obtained using a JEOL 1230 TEM.

TEM/STEM-EDX: Alloy particles were dropcast on silica nitride grids (76042-47, Electron Microscopy Sciences) and dried under ultrapure nitrogen in a desiccator. For the leached sample, the grid with deposited particles was immersed in 1.7 M HNO_3 for 45 minutes.

Brightfield TEM micrographs and STEM-EDX maps were obtained using a JEOL 2100 TEM operating at 200 kV.

Mie theory simulations: Mie theory calculations were carried out using a modified version of the MatScat functions (Copyright 2016, Jan Schäfer).[100] Published dielectric functions for gold-silver alloys were used.[101] A uniform refractive index of 1.5 was assumed based on a weighted average between ITO and water.

Numerical simulations of leaching profiles: An initial diameter of 100 nm and silver mole fraction of 0.8 were assumed and the gold content was calculated form the initial volume and initial mole fraction of the nanoparticle. Equation (3) was expressed as a function of volume (equation ES24) and the volume after a timestep of 1 minute was simulated using the average leaching rate constant found experimentally. The new silver mole fraction was calculated from the initial gold content and the new total volume of the nanoparticle. The calculation was iteratively repeated with the new mole fraction until the silver content reached zero. To simulate the leaching profile for the shrinking-particle model, the rate constant was held constant for all time steps (equation ES26).

ASSOCIATED CONTENT

Supporting Information: Additional information includes nanoparticle characterization (sections 1,8,9), stability of nanoparticles in water under illumination (section 2), Calculation of PCC (section 3), Kolmogorov–Smirnov Test (section 4), calculation of expected final nanoparticle size (section 5), effect of change in silver and change in size on the particle spectrum (section 6), wavelength changes during leaching (section 7), color images before and after leaching (section 10), additional leaching profiles (section 11), effect of particle size on initial leaching rate (section 12), calculation of the theoretical solubility limit (section 13), derivation of rate law (section 14), additional details about the simulation of leaching profiles

(section 15), alternative rate model with constant nanoparticle size (section 16), spectra of particles in 1.7 M nitric acid (section 17), histograms of nanoparticle size and composition after leaching in 1.7 M nitric acid (section 18), SEM after leaching in 1.7 M nitric acid (section 19), and additional STEM-EDX characterization of leached particles (section 20).

AUTHOR INFORMATION

Corresponding Authors:

*E-mail: cflandes@rice.edu

*E-mail: stephan.barcikowski@uni-due.de

*E-mail: slink@rice.edu

ORCID:

Alexander Al-Zubeidi: 0000-0001-8124-4661

Charlotte Flatebo: 0000-0002-1395-989X

Christoph Rehbock: 0000-0002-4708-5246

Seyyed Ali Hosseini Jebeli: 0000-0002-7327-0648

Stephan Barcikowski: 0000-0002-9739-7272

Christy F. Landes: 0000-0003-4163-6497

Stephan Link: 0000-0002-4781-930X

Notes:

The authors declare no competing financial interest.

ACKNOWLEDGMENTS

This work was primarily supported by the Army Research Office under fund number W911NF1910363, awarded to C.F.L and S.L. and supporting A.A.-Z. C.F. acknowledges support from a National Defense Science and Engineering Graduate Fellowship. We also acknowledge funding from the Robert A. Welch Foundation (C-1787 to C.F.L. and C-1664 to S.L.) and the National Science Foundation (Grant No. CHE-1727122 to S.L.). S.L. also thanks support from the Deutsche Forschungsgesellschaft for support as a Mercator Fellow. We also thank the Deutsche Forschungsgemeinschaft for funding the synthesis of the gold-silver alloy nanoparticles (BA 3580/16-1 to S.B.). This work was conducted in part using resources of the Shared Equipment Authority at Rice University.

REFERENCES

1. Jouyban, A.; Rahimpour, E., Optical Sensors Based on Silver Nanoparticles for Determination of Pharmaceuticals: An Overview of Advances in the Last Decade. *Talanta* **2020,** *217*, 121071.

2. Loza, K.; Heggen, M.; Epple, M., Synthesis, Structure, Properties, and Applications of Bimetallic Nanoparticles of Noble Metals. *Adv. Funct. Mater.* **2020,** *30*, 1909260.

3. Liu, X.-H.; Ma, J.-G.; Niu, Z.; Yang, G.-M.; Cheng, P., An Efficient Nanoscale Heterogeneous Catalyst for the Capture and Conversion of Carbon Dioxide at Ambient Pressure. *Angew. Chem. Int. Ed.* **2015,** *54*, 988-991.

4. Arora, N.; Mehta, A.; Mishra, A.; Basu, S., 4-Nitrophenol Reduction Catalysed by Au-Ag Bimetallic Nanoparticles Supported on LDH: Homogeneous *vs*. Heterogeneous Catalysis. *Appl. Clay Sci.* **2018,** *151*, 1-9.

5. Dong, X.-Y.; Gao, Z.-W.; Yang, K.-F.; Zhang, W.-Q.; Xu, L.-W., Nanosilver as a New Generation of Silver Catalysts in Organic Transformations for Efficient Synthesis of Fine Chemicals. *Catal. Sci. Technol.* **2015,** *5*, 2554-2574.

6. Grade, S.; Eberhard, J.; Neumeister, A.; Wagener, P.; Winkel, A.; Stiesch, M.; Barcikowski, S., Serum Albumin Reduces the Antibacterial and Cytotoxic Effects of Hydrogel-Embedded Colloidal Silver Nanoparticles. *RSC Adv.* **2012,** *2*, 7190-7196.

7. Grade, S.; Eberhard, J.; Wagener, P.; Winkel, A.; Sajti, C. L.; Barcikowski, S.; Stiesch, M., Therapeutic Window of Ligand-Free Silver Nanoparticles in Agar-Embedded and Colloidal State: *In Vitro* Bactericidal Effects and Cytotoxicity. *Adv. Eng. Mater.* **2012,** *14*, B231-B239.

8. Chernousova, S.; Epple, M., Silver as Antibacterial Agent: Ion, Nanoparticle, and Metal. *Angew. Chem. Int. Ed.* **2013,** *52*, 1636-1653.

9. Pelaz, B.; Alexiou, C.; Alvarez-Puebla, R. A.; Alves, F.; Andrews, A. M.; Ashraf, S.; Balogh, L. P.; Ballerini, L.; Bestetti, A.; Brendel, C.; Bosi, S.; Carril, M.; Chan, W. C. W.; Chen, C.; Chen, X.; Chen, X.; Cheng, Z.; Cui, D.; Du, J.; Dullin, C.*, et al.*, Diverse Applications of Nanomedicine. *ACS Nano* **2017,** *11*, 2313-2381.

10. Pal, S.; Yoon, E. J.; Tak, Y. K.; Choi, E. C.; Song, J. M., Synthesis of Highly Antibacterial Nanocrystalline Trivalent Silver Polydiguanide. *J. Am. Chem. Soc.* **2009,** *131*, 16147-16155.

11. Morones-Ramirez, J. R.; Winkler, J. A.; Spina, C. S.; Collins, J. J., Silver Enhances Antibiotic Activity against Gram-Negative Bacteria. *Sci. Transl. Med.* **2013,** *5*, 190ra181-190ra181.

12. Kumar, A.; Vemula, P. K.; Ajayan, P. M.; John, G., Silver-Nanoparticle-Embedded Antimicrobial Paints Based on Vegetable Oil. *Nat. Mater.* **2008,** *7*, 236-241.

13. Loza, K.; Diendorf, J.; Sengstock, C.; Ruiz-Gonzalez, L.; Gonzalez-Calbet, J. M.; Vallet-Regi, M.; Köller, M.; Epple, M., The Dissolution and Biological Effects of Silver Nanoparticles in Biological Media. *J. Mater. Chem. B* **2014,** *2*, 1634-1643.

14. Liu, J.; Sonshine, D. A.; Shervani, S.; Hurt, R. H., Controlled Release of Biologically Active Silver from Nanosilver Surfaces. *ACS Nano* **2010,** *4*, 6903-6913.

15. Ivask, A.; ElBadawy, A.; Kaweeteerawat, C.; Boren, D.; Fischer, H.; Ji, Z.; Chang, C. H.; Liu, R.; Tolaymat, T.; Telesca, D.; Zink, J. I.; Cohen, Y.; Holden, P. A.; Godwin, H. A., Toxicity Mechanisms in *Escherichia Coli* Vary for Silver Nanoparticles and Differ from Ionic Silver. *ACS Nano* **2014,** *8*, 374-386.

16. Dai, X.; Guo, Q.; Zhao, Y.; Zhang, P.; Zhang, T.; Zhang, X.; Li, C., Functional Silver Nanoparticle as a Benign Antimicrobial Agent that Eradicates Antibiotic-Resistant Bacteria and Promotes Wound Healing. *ACS Appl. Mater. Interfaces* **2016,** *8*, 25798-25807.

17. Hudson-Smith, N. V.; Clement, P. L.; Brown, R. P.; Krause, M. O. P.; Pedersen, J. A.; Haynes, C. L., Research Highlights: Speciation and Transformations of Silver Released From Ag NPs in Three Species. *Environ. Sci. Nano* **2016,** *3*, 1236-1240.

18. Kirmanidou, Y.; Sidira, M.; Bakopoulou, A.; Tsouknidas, A.; Prymak, O.; Papi, R.; Choli-Papadopoulou, T.; Epple, M.; Michailidis, N.; Koidis, P.; Michalakis, K., Assessment of Cytotoxicity and Antibacterial Effects of Silver Nanoparticle-Doped Titanium Alloy Surfaces. *Dent. Mater.* **2019,** *35*, e220-e233.

19. Stabryla, L. M.; Johnston, K. A.; Millstone, J. E.; Gilbertson, L. M., Emerging Investigator Series: It's Not All About the Ion: Support for Particle-Specific Contributions to Silver Nanoparticle Antimicrobial Activity. *Environ. Sci. Nano* **2018,** *5*, 2047-2068.

20. McQuillan, J. S.; Groenaga Infante, H.; Stokes, E.; Shaw, A. M., Silver Nanoparticle Enhanced Silver Ion Stress Response in *Escherichia Coli* K12. *Nanotoxicology* **2012,** *6*, 857-866.

21. Xiu, Z.-m.; Zhang, Q.-b.; Puppala, H. L.; Colvin, V. L.; Alvarez, P. J. J., Negligible Particle-Specific Antibacterial Activity of Silver Nanoparticles. *Nano Lett.* **2012,** *12*, 4271-4275.

22. Peretyazhko, T. S.; Zhang, Q.; Colvin, V. L., Size-Controlled Dissolution of Silver Nanoparticles at Neutral and Acidic pH Conditions: Kinetics and Size Changes. *Environ. Sci. Technol.* **2014,** *48*, 11954-11961.

23. Zhang, W.; Yao, Y.; Sullivan, N.; Chen, Y., Modeling the Primary Size Effects of Citrate-Coated Silver Nanoparticles on their Ion Release Kinetics. *Environ. Sci. Technol.* **2011,** *45*, 4422-4428.

24. AshaRani, P. V.; Low Kah Mun, G.; Hande, M. P.; Valiyaveettil, S., Cytotoxicity and Genotoxicity of Silver Nanoparticles in Human Cells. *ACS Nano* **2009,** *3*, 279-290.

25. Park, M. V.; Neigh, A. M.; Vermeulen, J. P.; de la Fonteyne, L. J.; Verharen, H. W.; Briedé, J. J.; van Loveren, H.; de Jong, W. H., The Effect of Particle Size on the Cytotoxicity, Inflammation, Developmental Toxicity and Genotoxicity of Silver Nanoparticles. *Biomaterials* **2011,** *32*, 9810-9817.

26. Kumar, S.; Majhi, R. K.; Singh, A.; Mishra, M.; Tiwari, A.; Chawla, S.; Guha, P.; Satpati, B.; Mohapatra, H.; Goswami, L.; Goswami, C., Carbohydrate-Coated Gold–Silver Nanoparticles for Efficient Elimination of Multidrug Resistant Bacteria and *in Vivo* Wound Healing. *ACS Appl. Mater. Interfaces* **2019,** *11*, 42998-43017.

27. Panicker, S.; Ahmady, I. M.; Han, C.; Chehimi, M.; Mohamed, A. A., On Demand Release of Ionic Silver from Gold-Silver Alloy Nanoparticles: Fundamental Antibacterial Mechanisms Study. *Mater. Today Chem.* **2020,** *16*, 100237.

28. Long, Y.-M.; Hu, L.-G.; Yan, X.-T.; Zhao, X.-C.; Zhou, Q.-F.; Cai, Y.; Jiang, G.-B., Surface Ligand Controls Silver Ion Release of Nanosilver and its Antibacterial Activity Against Escherichia Coli. *Int. J. Nanomedicine* **2017,** *12*, 3193-3206.

29. Xu, M.; Liu, J.; Xu, X.; Liu, S.; Peterka, F.; Ren, Y.; Zhu, X., Synthesis and Comparative Biological Properties of Ag-PEG Nanoparticles with Tunable Morphologies from Janus to Multi-Core Shell Structure. *Materials* **2018,** *11*, 1787.

30. Tiedemann, D.; Taylor, U.; Rehbock, C.; Jakobi, J.; Klein, S.; Kues, W. A.; Barcikowski, S.; Rath, D., Reprotoxicity of Gold, Silver, and Gold–Silver Alloy Nanoparticles on Mammalian Gametes. *Analyst* **2014,** *139*, 931-942.

31. Taylor, U.; Tiedemann, D.; Rehbock, C.; Kues, W. A.; Barcikowski, S.; Rath, D., Influence of Gold, Silver and Gold-Silver Alloy Nanoparticles on Germ Cell Function and Embryo Development. *Beilstein. J. Nanotechnol.* **2015,** *6*, 651-664.

32. Jena, P.; Bhattacharya, M.; Bhattacharjee, G.; Satpati, B.; Mukherjee, P.; Senapati, D.; Srinivasan, R., Bimetallic Gold–Silver Nanoparticles Mediate Bacterial Killing by Disrupting the Actin Cytoskeleton MreB. *Nanoscale* **2020,** *12*, 3731-3749.

33. Padmos, J. D.; Langman, M.; MacDonald, K.; Comeau, P.; Yang, Z.; Filiaggi, M.; Zhang, P., Correlating the Atomic Structure of Bimetallic Silver–Gold Nanoparticles to their Antibacterial and Cytotoxic Activities. *J. Phys. Chem. C* **2015,** *119*, 7472-7482.

34. Wang, Y.; Wan, J.; Miron, R. J.; Zhao, Y.; Zhang, Y., Antibacterial Properties and Mechanisms of Gold–Silver Nanocages. *Nanoscale* **2016,** *8*, 11143-11152.

35. Chang, Y.; Cheng, Y.; Feng, Y.; Li, K.; Jian, H.; Zhang, H., Upshift of the d Band Center toward the Fermi Level for Promoting Silver Ion Release, Bacteria Inactivation, and Wound Healing of Alloy Silver Nanoparticles. *ACS Appl. Mater. Interfaces* **2019,** *11*, 12224-12231.

36. Gao, C.; Hu, Y.; Wang, M.; Chi, M.; Yin, Y., Fully Alloyed Ag/Au Nanospheres: Combining the Plasmonic Property of Ag with the Stability of Au. *J. Am. Chem. Soc.* **2014,** *136*, 7474-7479.

37. Grade, S.; Eberhard, J.; Jakobi, J.; Winkel, A.; Stiesch, M.; Barcikowski, S., Alloying Colloidal Silver Nanoparticles With Gold Disproportionally Controls Antibacterial and Toxic Effects. *Gold Bull.* **2014,** *47*, 83-93.

38. Martínez, L. L.; Segarra, M.; Fernández, M.; Espiell, F., Kinetics of the Dissolution of Pure Silver and Silver-Gold Alloys in Nitric Acid Solution. *Metall. Mater. Trans.* **1993,** *24*, 827-837.

39. Sotiriou, G. A.; Etterlin, G. D.; Spyrogianni, A.; Krumeich, F.; Leroux, J.-C.; Pratsinis, S. E., Plasmonic Biocompatible Silver–Gold Alloyed Nanoparticles. *Chem. Comm.* **2014,** *50*, 13559-13562.

40. Sheldon, M. T.; van de Groep, J.; Brown, A. M.; Polman, A.; Atwater, H. A., Plasmoelectric Potentials in Metal Nanostructures. *Science* **2014,** *346*, 828-831.

41. Hu, M.; Chen, J.; Li, Z.-Y.; Au, L.; Hartland, G. V.; Li, X.; Marquez, M.; Xia, Y., Gold Nanostructures: Engineering their Plasmonic Properties for Biomedical Applications. *Chem. Soc. Rev.* **2006,** *35*, 1084-1094.

42. Brongersma, M. L.; Halas, N. J.; Nordlander, P., Plasmon-Induced Hot Carrier Science and Technology. *Nat. Nanotechnol.* **2015,** *10*, 25-34.

43. Rioux, D.; Meunier, M., Seeded Growth Synthesis of Composition and Size-Controlled Gold–Silver Alloy Nanoparticles. *J. Phys. Chem. C* **2015,** *119*, 13160-13168.

44. Rehn, S. M.; Ringe, E., Controllably Hollow AgAu Nanoparticles *via* Nonaqueous, Reduction Agent-Assisted Galvanic Replacement. *Part. Part. Sys. Char.* **2018,** *35*, 1700381.

45. Mallin, M. P.; Murphy, C. J., Solution-Phase Synthesis of sub-10 nm Au−Ag Alloy Nanoparticles. *Nano Lett.* **2002,** *2*, 1235-1237.

46. Zhao, J.; Nguyen, S. C.; Ye, R.; Ye, B.; Weller, H.; Somorjai, G. A.; Alivisatos, A. P.; Toste, F. D., A Comparison of Photocatalytic Activities of Gold Nanoparticles Following Plasmonic and Interband Excitation and a Strategy for Harnessing Interband Hot Carriers for Solution Phase Photocatalysis. *ACS Cent. Sci.* **2017,** *3*, 482-488.

47. Grillet, N.; Manchon, D.; Cottancin, E.; Bertorelle, F.; Bonnet, C.; Broyer, M.; Lermé, J.; Pellarin, M., Photo-Oxidation of Individual Silver Nanoparticles: A Real-Time Tracking of Optical and Morphological Changes. *J. Phys. Chem. C* **2013,** *117*, 2274-2282.

48. Goodman, A. M.; Cao, Y.; Urban, C.; Neumann, O.; Ayala-Orozco, C.; Knight, M. W.; Joshi, A.; Nordlander, P.; Halas, N. J., The Surprising *in Vivo* Instability of Near-IR-Absorbing Hollow Au–Ag Nanoshells. *ACS Nano* **2014,** *8*, 3222-3231.

49. Nishi, H.; Tatsuma, T., Photoregulated Nanopore Formation *via* Plasmon-Induced Dealloying of Au–Ag Alloy Nanoparticles. *J. Phys. Chem. C* **2017,** *121*, 2473-2480.

50. Cheng, J.; Bordes, R.; Olsson, E.; Holmberg, K., One-Pot Synthesis of Porous Gold Nanoparticles by Preparation of Ag/au Nanoparticles Followed by Dealloying. *Colloids Surf. A* **2013,** *436*, 823-829.

51. Li, X.; Lenhart, J. J., Aggregation and Dissolution of Silver Nanoparticles in Natural Surface Water. *Environ. Sci. Technol.* **2012,** *46*, 5378-5386.

52. Huynh, K. A.; Chen, K. L., Aggregation Kinetics of Citrate and Polyvinylpyrrolidone Coated Silver Nanoparticles in Monovalent and Divalent Electrolyte Solutions. *Environ. Sci. Technol.* **2011,** *45*, 5564-5571.

53. Kumar, A.; Villarreal, E.; Zhang, X.; Ringe, E., Micro-Extinction Spectroscopy (MExS): A Versatile Optical Characterization Technique. *Adv. Struct. Chem. Imag.* **2018,** *4*, 8.

54. Foerster, B.; Hartelt, M.; Collins, S. S. E.; Aeschlimann, M.; Link, S.; Sönnichsen, C., Interfacial States Cause Equal Decay of Plasmons and Hot Electrons at Gold–Metal Oxide Interfaces. *Nano Lett.* **2020,** *20*, 3338-3343.

55. Becker, J.; Schubert, O.; Sönnichsen, C., Gold Nanoparticle Growth Monitored *in Situ* Using a Novel Fast Optical Single-Particle Spectroscopy Method. *Nano Lett.* **2007,** *7*, 1664-1669.

56. Al-Zubeidi, A.; Hoener, B. S.; Collins, S. S. E.; Wang, W.; Kirchner, S. R.; Hosseini Jebeli, S. A.; Joplin, A.; Chang, W.-S.; Link, S.; Landes, C. F., Hot Holes Assist Plasmonic Nanoelectrode Dissolution. *Nano Lett.* **2019,** *19*, 1301-1306.

57. Carattino, A.; Khatua, S.; Orrit, M., *In Situ* Tuning of Gold Nanorod Plasmon Through Oxidative Cyanide Etching. *Phys. Chem. Chem. Phys.* **2016,** *18*, 15619-15624.

58. Hu, S.; Yi, J.; Zhang, Y.-J.; Lin, K.-Q.; Liu, B.-J.; Chen, L.; Zhan, C.; Lei, Z.-C.; Sun, J.-J.; Zong, C.; Li, J.-F.; Ren, B., Observing Atomic Layer Electrodeposition on Single Nanocrystals Surface by Dark Field Spectroscopy. *Nat. Commun.* **2020,** *11*, 2518.

59. Collins, S. S. E.; Wei, X.; McKenzie, T. G.; Funston, A. M.; Mulvaney, P., Single Gold Nanorod Charge Modulation in an Ion Gel Device. *Nano Lett.* **2016,** *16*, 6863-6869.

60. Sundaresan, V.; Monaghan, J. W.; Willets, K. A., Visualizing the Effect of Partial Oxide Formation on Single Silver Nanoparticle Electrodissolution. *J. Phys. Chem. C* **2018,** *122*, 3138-3145.

61. Zhang, D.; Gökce, B.; Barcikowski, S., Laser Synthesis and Processing of Colloids: Fundamentals and Applications. *Chem. Rev.* **2017,** *117*, 3990-4103.

62. Streubel, R.; Barcikowski, S.; Gökce, B., Continuous Multigram Nanoparticle Synthesis by High-Power, High-Repetition-Rate Ultrafast Laser Ablation in Liquids. *Opt. Lett.* **2016,** *41*, 1486-1489.

63. Streubel, R.; Bendt, G.; Gökce, B., Pilot-Scale Synthesis of Metal Nanoparticles by High-Speed Pulsed Laser Ablation in Liquids. *Nanotechnology* **2016,** *27*, 205602.

64. Lee, I.; Han, S. W.; Kim, K., Production of Au–ag Alloy Nanoparticles by Laser Ablation of Bulk Alloys. *Chem. Comm.* **2001**, 1782-1783.

65. Neumeister, A.; Jakobi, J.; Rehbock, C.; Moysig, J.; Barcikowski, S., Monophasic Ligand-Free Alloy Nanoparticle Synthesis Determinants During Pulsed Laser Ablation of

Bulk Alloy and Consolidated Microparticles in Water. *Phys. Chem. Chem. Phys.* **2014,** *16*, 23671-23678.

66. Pfeiffer, C.; Rehbock, C.; Hühn, D.; Carrillo-Carrion, C.; de Aberasturi, D. J.; Merk, V.; Barcikowski, S.; Parak, W. J., Interaction of Colloidal Nanoparticles with their Local Environment: The (Ionic) Nanoenvironment around Nanoparticles is Different from Bulk and Determines the Physico-Chemical Properties of the Nanoparticles. *J. R. Soc. Interface* **2014,** *11*, 20130931-20130931.

67. Hahn, A.; Fuhlrott, J.; Loos, A.; Barcikowski, S., Cytotoxicity and Ion Release of Alloy Nanoparticles. *J. Nanopart. Res.* **2012,** *14*, 1-10.

68. Prymak, O.; Jakobi, J.; Rehbock, C.; Epple, M.; Barcikowski, S., Crystallographic Characterization of Laser-Generated, Polymer-Stabilized 4 nm Silver-Gold Alloyed Nanoparticles. *Mater. Chem. Phys.* **2018,** *207*, 442-450.

69. Messina, G. C.; Wagener, P.; Streubel, R.; De Giacomo, A.; Santagata, A.; Compagnini, G.; Barcikowski, S., Pulsed Laser Ablation of a Continuously-Fed Wire in Liquid Flow for High-Yield Production of Silver Nanoparticles. *Phys. Chem. Chem. Phys.* **2013,** *15*, 3093-3098.

70. Shopa, M.; Kolwas, K.; Derkachova, A.; Derkachov, G., Dipole and Quadrupole Surface Plasmon Resonance Contributions in Formation of Near-Field Images of a Gold Nanosphere. *Opto-Electron. Rev.* **2010,** *18*, 421-428.

71. Krekeler, T.; Straßer, A. V.; Graf, M.; Wang, K.; Hartig, C.; Ritter, M.; Weissmüller, J., Silver-Rich Clusters in Nanoporous Gold. *Mater. Res. Lett.* **2017,** *5*, 314-321.

72. Li, X.; Chen, Q.; McCue, I.; Snyder, J.; Crozier, P.; Erlebacher, J.; Sieradzki, K., Dealloying of Noble-Metal Alloy Nanoparticles. *Nano Lett.* **2014,** *14*, 2569-2577.

73. Wonner, K.; Rurainsky, C.; Tschulik, K., Operando Studies of the Electrochemical Dissolution of Silver Nanoparticles in Nitrate Solutions Observed With Hyperspectral Dark-Field Microscopy. *Front. Chem.* **2020,** *7*, 912.

74. Zhao, J.; Pinchuk, A. O.; Mcmahon, J. M.; Li, S. Z.; Ausman, L. K.; Atkinson, A. L.; Schatz, G. C., Methods for Describing the Electromagnetic Properties of Silver and Gold Nanoparticles. *Accounts Chem. Res.* **2008,** *41*, 1710-1720.

75. Pickering, H. W., Characteristic Features of Alloy Polarization Curves. *Corros. Sci.* **1983,** *23*, 1107-1120.

76. Hahn, A.; Günther, S.; Wagener, P.; Barcikowski, S., Electrochemistry-Controlled Metal Ion Release From Silicone Elastomer Nanocomposites Through Combination of Different Metal Nanoparticles. *J. Mater. Chem.* **2011,** *21*, 10287-10289.

77. Hahn, A.; Brandes, G.; Wagener, P.; Barcikowski, S., Metal Ion Release Kinetics From Nanoparticle Silicone Composites. *J. Control. Release* **2011,** *154*, 164-170.

78. Ma, R.; Levard, C.; Marinakos, S. M.; Cheng, Y.; Liu, J.; Michel, F. M.; Brown, G. E.; Lowry, G. V., Size-Controlled Dissolution of Organic-Coated Silver Nanoparticles. *Environ. Sci. Technol.* **2012,** *46*, 752-759.

79. Jiang, J.; Oberdörster, G.; Elder, A.; Gelein, R.; Mercer, P.; Biswas, P., Does Nanoparticle Activity Depend Upon Size and Crystal Phase? *Nanotoxicology* **2008,** *2*, 33-42.

80. Brunner, T. J.; Grass, R. N.; Bohner, M.; Stark, W. J., Effect of Particle Size, Crystal Phase and Crystallinity on the Reactivity of Tricalcium Phosphate Cements for Bone Reconstruction. *J. Mater. Chem.* **2007,** *17*, 4072-4078.

81. Kittler, S.; Greulich, C.; Diendorf, J.; Köller, M.; Epple, M., Toxicity of Silver Nanoparticles Increases during Storage because of Slow Dissolution under Release of Silver Ions. *Chem. Mater.* **2010,** *22*, 4548-4554.

82. Zhang, C.; Hu, Z.; Deng, B., Silver Nanoparticles in Aquatic Environments: Physiochemical Behavior and Antimicrobial Mechanisms. *Water Res.* **2016,** *88*, 403-427.

83. Seidell, A., *Solubilities of Inorganic and Organic Compounds; a Compilation of Quantitative Solubility Data From the Periodical Literature*. Second Edition ed.; D. van Nostrand Company Inc: New York, 1919.

84. Nanta, P.; Skolpap, W.; Kasemwong, K.; Shimoyama, Y., Development of a Diffusion-Limited Shrinking Particle Model of Cellulose Dissolution in a Carbon Dioxide Switchable System. *Chem. Eng. Sci.* **2018,** *179*, 214-220.

85. Han, K. N.; Fuerstenau, M. C., Dissolution Behavior of Metals From Binary Alloys. *Int. J. Miner. Process.* **2003,** *72*, 355-364.

86. Rugolo, J.; Erlebacher, J.; Sieradzki, K., Length Scales in Alloy Dissolution and Measurement of Absolute Interfacial Free Energy. *Nat. Mater.* **2006,** *5*, 946-949.

87. Mahl, D.; Diendorf, J.; Ristig, S.; Greulich, C.; Li, Z.-A.; Farle, M.; Köller, M.; Epple, M., Silver, Gold, and Alloyed Silver–Gold Nanoparticles: Characterization and Comparative Cell-Biologic Action. *J. Nanoparticle Res.* **2012,** *14*, 1153.

88. Schade, O. R.; Stein, F.; Reichenberger, S.; Gaur, A.; Saraçi, E.; Barcikowski, S.; Grunwaldt, J.-D., Selective Aerobic Oxidation of 5-(Hydroxymethyl)furfural over Heterogeneous Silver-Gold Nanoparticle Catalysts. *Adv. Synth. Catal.* **2020,** *362*, 5681-5696.

89. Grasmik, V.; Rurainsky, C.; Loza, K.; Evers, M. V.; Prymak, O.; Heggen, M.; Tschulik, K.; Epple, M., Deciphering the Surface Composition and the Internal Structure of Alloyed Silver–Gold Nanoparticles. *Chem. Eur. J.* **2018,** *24*, 9051-9060.

90. Han, K. N., Factors Affecting the Dissolution Behavior of Metals from Binary Alloys. *J. Korean Inst. Resour. Recycl.* **2001,** *10*, 49-55.

91. Safari, V.; Arzpeyma, G.; Rashchi, F.; Mostoufi, N., A Shrinking Particle-Shrinking Core Model for Leaching of a Zinc Ore Containing Silica. *Int. J. Miner. Process.* **2009,** *93*, 79-83.

92. Cho, E. C.; Cobley, C. M.; Rycenga, M.; Xia, Y., Fine Tuning the Optical Properties of Au–Ag Nanocages by Selectively Etching Ag with Oxygen and a Water-soluble Thiol. *J. Mater. Chem.* **2009,** *19*, 6317-6320.

93. Rurainsky, C.; Manjón, A. G.; Hiege, F.; Chen, Y.-T.; Scheu, C.; Tschulik, K., Electrochemical Dealloying as a Tool to Tune the Porosity, Composition and Catalytic Activity of Nanomaterials. *J. Mater. Chem. A* **2020,** *8*, 19405-19413.

94. Arifuzzaman, M.; Millhouse, P. W.; Raval, Y.; Pace, T. B.; Behrend, C. J.; Behbahani, S. B.; DesJardins, J. D.; Tzeng, T.-R. J.; Anker, J. N., An Implanted pH Sensor Read Using Radiography. *Analyst* **2019,** *144*, 2984-2993.

95. Ribeiro, M.; Monteiro, F. J.; Ferraz, M. P., Infection of Orthopedic Implants with Emphasis on Bacterial Adhesion Process and Techniques Used in Studying Bacterial-Material Interactions. *Biomatter* **2012,** *2*, 176-194.

96. Nel, A. E.; Mädler, L.; Velegol, D.; Xia, T.; Hoek, E. M.; Somasundaran, P.; Klaessig, F.; Castranova, V.; Thompson, M., Understanding Biophysicochemical Interactions at the Nano–Bio Interface. *Nat. Mater.* **2009,** *8*, 543-557.

97. Kurylowicz, M.; Giuliani, M.; Dutcher, J. R., Using Nanoscale Substrate Curvature to Control the Dimerization of a Surface-Bound Protein. *ACS Nano* **2012,** *6*, 10571-10580.

98. Lawrence, R. E.; Zoncu, R., The Lysosome as a Cellular Centre for Signalling, Metabolism and Quality Control. *Nat. Cell Biol.* **2019,** *21*, 133-142.

99. Weber, R. A.; Yen, F. S.; Nicholson, S. P.; Alwaseem, H.; Bayraktar, E. C.; Alam, M.; Timson, R. C.; La, K.; Abu-Remaileh, M.; Molina, H., Maintaining Iron Homeostasis

is the Key Role of Lysosomal Acidity for Cell Proliferation. *Mol. Cell* **2020,** *77*, 645-655. e647.

100. Schäfer, J.; Lee, S. C.; Kienle, A., Calculation of the Near Fields for the Scattering of Electromagnetic Waves by Multiple Infinite Cylinders at Perpendicular Incidence. *J. Quant. Spectrosc. Radiat. Transf.* **2012,** *113*, 2113-2123.

101. Rioux, D.; Vallières, S.; Besner, S.; Muñoz, P.; Mazur, E.; Meunier, M., An Analytic Model for the Dielectric Function of Au, Ag, and their Alloys. *Adv. Opt. Mater.* **2014,** *2*, 176-182.

TOC Figure: